

Decomposition-based and Interference Perception for Infrared and Visible Image Fusion in Complex Scenes

Xilai Li Xiaosong Li* Haishu Tan

School of Physics and Optoelectronic Engineering, Foshan University, Foshan 528225, China

20210300236@stu.fosu.edu.cn, lixiaosong@buaa.edu.cn

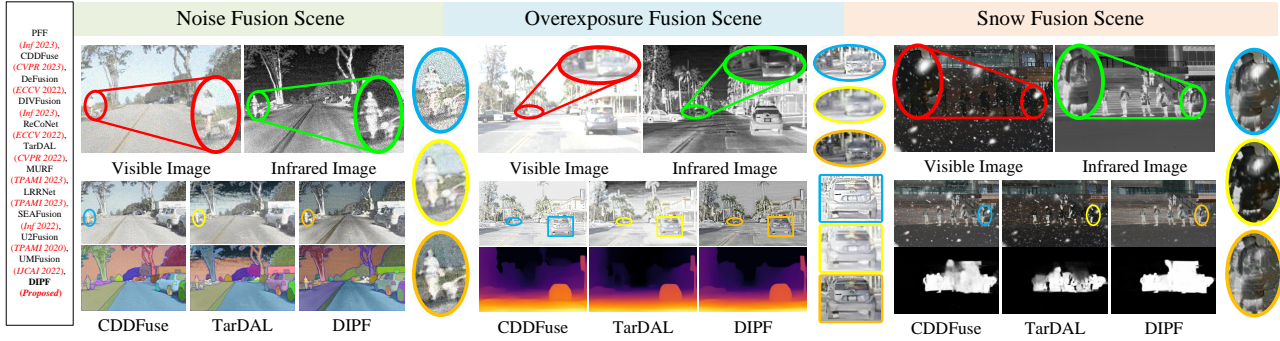


Figure 1. Visual comparisons of different fusion methods in various complex scenes, including three downstream tasks: semantic segmentation, depth estimation, and salient object detection. The compared methods in experiments are listed on the far left.

Abstract

Infrared and visible image fusion has emerged as a prominent research in computer vision. However, little attention has been paid on complex scenes fusion, causing existing techniques to produce sub-optimal results when suffers from real interferences. To fill this gap, we propose a decomposition-based and interference perception image fusion method. Specifically, we classify the pixels of visible image from the degree of scattering of light transmission, based on which we then separate the detail and energy information of the image. This refined decomposition facilitates the proposed model in identifying more interfering pixels that are in complex scenes. To strike a balance between denoising and detail preservation, we propose an adaptive denoising scheme for fusing detail components. Meanwhile, we propose a new weighted fusion rule by considering the distribution of image energy information from the perspective of multiple directions. Extensive experiments in complex scenes fusions cover adverse weathers, noise, blur, overexposure, fire, as well as downstream tasks including semantic segmentation, object detection, salient object detection and depth estimation, consistently indicate the effectiveness and superiority of the proposed method compared

with the recent representative methods.

1. Introduction

Infrared and visible image fusion (IVIF) [22, 28, 42, 54, 60] is utilized to enhance the quality of captured images by amalgamating complementary information from both spectral ranges. Infrared imaging excels in temperature detection and hidden object identification through thermal radiation but lacks color and has lower resolution. Visible imaging offers high detail and rich colors but struggles in low light and adverse conditions. IVIF overcomes these limitations, yielding comprehensive fused images. The fused images can enhance scene observation and comprehension for various downstream tasks, including semantic segmentation [12, 19], object detection [2, 3, 48], salient object detection [24, 35], and depth estimation [47, 50].

The existing IVIF methods can be broadly classified into deep learning (DL)-based [7, 16, 17, 31, 44, 45, 49] and traditional methods [13, 25, 27, 33, 34, 59, 63]. DL-based methods are roughly divided into Auto-Encoder (AE)-based [4, 15, 60], generative adversarial network (GAN)-based [22, 29, 30, 61], and convolutional neural network (CNN)-based methods [52, 57, 58]. AE manners use an encoder and decoder for feature extraction and image reconstruct-

*Corresponding author.

tion. The encoder captures features from infrared or visible images, which are then processed by a shared decoder for deep feature learning. In GAN-based methods, fusion is treated as an adversarial process where the generator combines features from two source images, guided by the discriminator to enhance informative details. The last type, CNN, extracts diverse features from input images through its hierarchical structure.

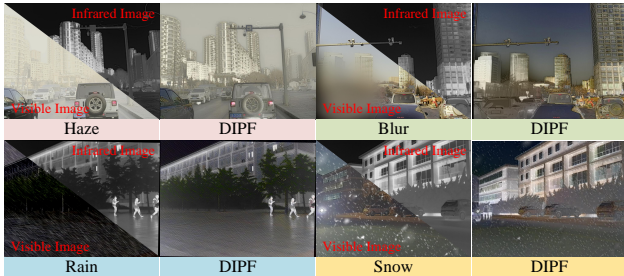


Figure 2. A fusion scene under weather disturbance, where Blur represents a scene where the sensor is destroyed by raindrops.

1.1. Motivation

These latest methods [21, 22, 42, 44, 60, 63] undoubtedly yielded the eye-catching performance. Nevertheless, one practical issue should be noticed, existing IVIF techniques potentially assume that fusion is conducted in high-quality scenes, such as normal sunny days, homogeneous lighting, etc. But the real situation is that in tasks such as automatic driving, scene analysis and interpretation, complex environmental interferences, such as extreme weather, blur, noise, overexposure, fire, etc., are often encountered, which may be single or multiple interferences simultaneously. Fig. 2 shows the fusion scenes when the visible sensor lens suffers from adverse weather. These practical requirements force that IVIF technology should have the ability to resist complex environmental interferences and achieve high-quality multi-modality image fusion under multi-interference conditions. To address this issue, we propose an IVIF method for complex environment with multiple interferences. **To the best of our knowledge, this is the first time that the IVIF addresses the complex scenes fusion problems.** Our main contributions as follows:

- 1) We propose a novel framework for IVIF, explicitly engineered to solve complex and challenging scenes. Our method adaptively identifies and processes interfering information in the source images, facilitating high-quality fusion even in extreme environments such as haze, noise, and heavy rain and fire.
- 2) We propose a light transmission-aware decomposition model that can accurately classify interfering pixels within complex scenes. Moreover, we develop an adaptive denoising scheme for high-frequency components,

achieving a balance between noise reduction and detail-preservation.

- 3) To emulate a wide array of intricate scenes encountered in real-world settings, we intentionally degrade the source images to varying extents. Our experiments show that our algorithm successfully fuses images under severe conditions, outperforming many current methods.

2. Related Work

2.1. Existing IVIF Methods

In recent years, DL has advanced the field of IVIF, with many researchers focusing on DL-based methods. Some DL-based algorithms [16, 20, 21, 39, 52, 60] have achieved good results in capturing multi-modality image information, and they usually design complex neural network structures and loss functions according to the needs of a specific task; however, such data-driven algorithms may fail in front of encountering unseen data and do not have strong generalizability. With the gradual improvement of a single IVIF task, many IVIF algorithms [10, 14, 18, 22, 42–44, 53] challenge partial downstream tasks (semantic segmentation, object detection, etc.) and complex scenes (haze, noise, and overexposure, etc.) by giving the algorithms multi-tasking capabilities, and this is bound to be the trend of future IVIF development. However, due to the lack of data and the increase of training difficulty, almost no algorithm is able to deal with multiple extreme scenes at one time in complex scenes. Due to its rigorous mathematical theory support, the traditional IVIF model may be able to fill this part of the gap, the traditional model does not need a large amount of data training. We can hinder the distribution of details in the complex scene, affecting the visual perception of the human eye pixels uniformly as interference pixels. Nonetheless, current research in this area is insufficient.

3. Proposed complex scenes fusion model

This section describes the flow of the proposed algorithm in detail. The general process is shown in Fig. 3.

3.1. Multi-component Decomposition

3.1.1 Transmission Map Estimation

A transmission map quantifies light absorption and scattering during its path from the scene to the camera, showing how light weakens. It not only estimates pixel transmittance but also emphasizes high-contrast and luminous areas like the sky, streetlights, and headlights in real-world images. These regions usually have high transmittance and are less affected by atmospheric scattering.

Step 1. Coarse transmission map acquisition

Assuming equal transmittance and atmospheric light across color channels in the input visible source image, the small-

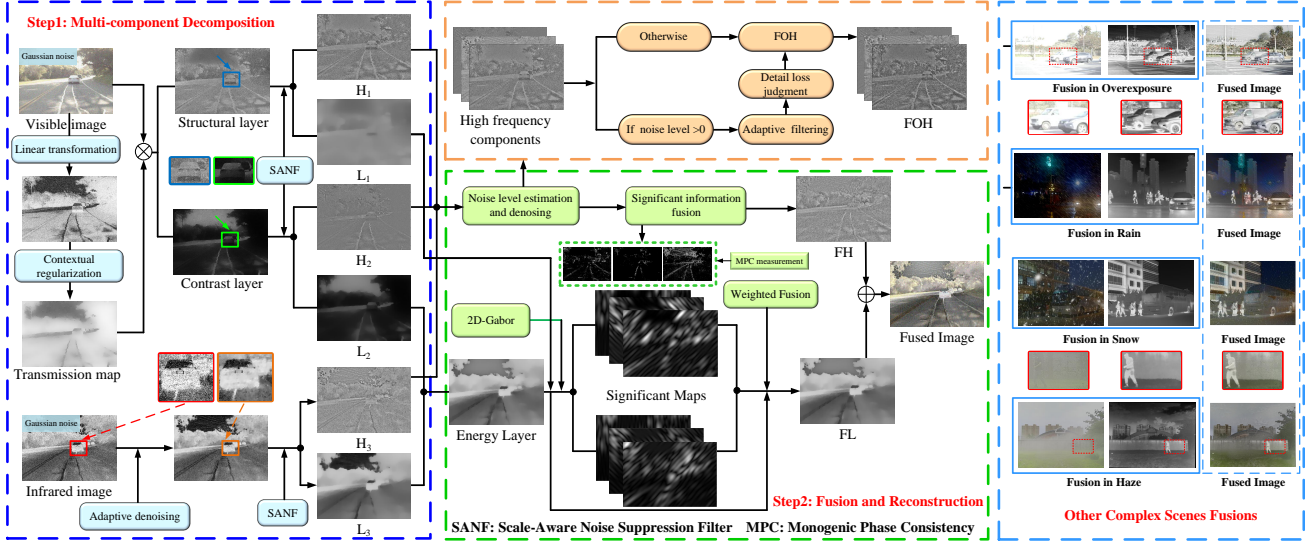


Figure 3. Overall framework of the proposed method, which contains two main steps: multi-component decomposition and feature fusion and reconstruction. The rightmost region shows four complex scenes fusion examples.

est channel provides a more precise identify the amount of noise [37]. The transmission map t is then calculated by:

$$t(x, y) = \frac{\min A - \min I(x, y)}{\min A - \min J(x, y)} \quad (1)$$

where $\min I(x, y)$, $\min J(x, y)$ and $\min A$ denote the minimum color channels for haze, clear images and atmospheric light, respectively. This process is implemented by minimum filter. The conventional atmospheric scattering model focuses on defogging by recovering a clear image J from a foggy image I . However, in real-life situations, complex scenes, including overexposure, snow and rainy conditions, also affect light scattering, posing greater challenges in J recovery. Our proposed algorithm only decomposes images based on light transmittance. To minimize the impact of J estimation errors on the transmittance map t , we reformulated the atmospheric scattering model as:

$$t(x, y) = (\min A - \min I(x, y)) \frac{\min A}{\min A - \min J(x, y)} \quad (2)$$

where $\min A$ is solved by dark channel prior [8]. If $\min J(x, y)$ is known, $t(x, y)$ can be obtained. Due to the positive correlation between $\min I(x, y)$ and $\min J(x, y)$ [51], $\min J(x, y)$ can be written as:

$$\min J(x, y) = \frac{1}{\ln(\min A - \min I(x, y))^\beta} \quad (3)$$

To find $\min J(x, y)$, we determine β using the least squares algorithm, which minimizes the sum of squared errors. We train our algorithm with a dataset [1] of 50 image pairs, haze and haze-free. According to least squares algorithm, we

calculate the value of β as 1.2778. Fig. 4 shows the comparison of transmission maps estimated by different models. It can be seen that the proposed model has relatively accurate transmission estimation performance under four scenes: rain, fog, snow and overexposure.

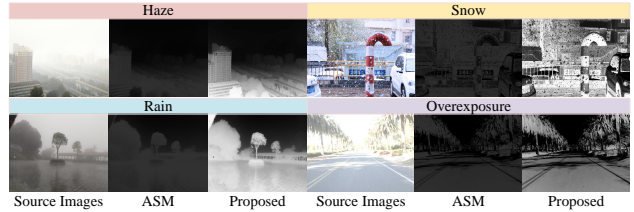


Figure 4. The light transmittance estimation is compared between the proposed and the atmospheric scattering model. ASM: Atmospheric Scattering Model.

Step 2. Transmission map optimization

The transmission map, derived from scene pixel depth estimation, is sensitive to errors and noise. To enhance its robustness, we introduced a contextual regularization-based image smoothing function [32] to optimize it:

$$\frac{\lambda}{2} \|t - \hat{t}\|_2^2 + \sum_{j \in \omega} \|W_j \circ (D_j \otimes t)\|_1 \quad (4)$$

where \hat{t} represents the smoothed transmission map, λ stands for the regularization parameter, ω is an index set [32], D_j denotes the differential operator, \circ represents the multiplicative operator, \otimes signifies the convolution operator, and W_j is the weight matrix of the filter as specified in [32]. To

improve the smoothing function, we adaptively adjusted λ based on noise level measurement [9] and $\lambda = 1.5 \times e^{-\sigma}$, where σ indicates the noise level. This adaptation decreases computational complexity and retains edge details while effectively suppressing noise.

3.1.2 Contrast and Structure Layers Decomposition

Since the transmission map can reflect the scattering information of the scene light, We use it to decompose the visible image into the contrast layer (CL) and structure layer (SL).

$$CL(x, y) = I_{\text{vis}}(x, y) \cdot (1 - t(x, y)) \quad (5)$$

$$SL(x, y) = I_{\text{vis}}(x, y) \cdot t(x, y) \quad (6)$$

This strategy distinguishes elements in a complex scene (e.g., overexposed areas, smoke, noise), aiding in the subsequent suppression and processing of interfering pixels.

3.1.3 High and Low Frequency Decomposition

Edge-preserving filters reduce noise and preserve edge information, improving the fused image quality. Zhou et al. [62] proposed a weighted least-squares optimization framework for this purpose. However, noise in the source image can mask feature information at higher scales, impacting scale perception metrics. To solve this, we use the Sobel operator for gradient detection in eight directions to create new weights. This strategy optimizes the basic framework of the above filters and the SANF is represented as follows:

$$\sum_p ((O^d(p) - I(p))^2 + \frac{\kappa}{\xi_p^{d-1} G_p^{d-1} Q_{r,p} S_p^{d-1} + \epsilon} ((\partial_x O^d)^2_p + (\partial_y O^d)^2_p)) \quad (7)$$

where O^d signifies the filtered result after the d -th iteration, with d take the value of 3, $Q_{r,p}$ is the scale-aware metric used to suppress image structures with spatial scales smaller than r , G_p^{d-1} is the bootstrap gradient, and ξ_p^{d-1} is the penalty coefficient. More detailed information about this filter can be found in [62]. Additionally, S_p denotes the noise suppression weight, which is calculated as follows.

$$S_p = \sqrt{\sum_{D=1}^8 \frac{1}{8} \times GL_p^D} \quad (8)$$

where D denotes the number of Sobel operator templates in different directions, and GL is the gradient map of the Sobel operator detected in different directions. Finally, the SANF process can thus be represented by $\text{SANF}(I, \kappa, r)$, where r is set to 1, and the weight value κ is used to modulate the degree of image smoothing.

Infrared images have lower resolution and are susceptible to noise due to weak signals and atmospheric interference. When infrared images suffer from noise interference, noise reduction is prioritized over texture preservation, which can improve fusion quality. Assuming that the noise level σ_{ir} of the infrared image is greater than 0, we filter it using the SANF, and $\kappa = 0.01 \cdot \log_5(\sigma_{ir})$.

After obtaining CL , SL , and the pre-processed infrared image \bar{I}_{ir} , we decompose them using SAMF into low-frequency (L_α) and high-frequency (H_α) components, where $\alpha \in \{1, 2, 3\}$ corresponds to CL , SL and \bar{I}_{ir} , respectively, and $\kappa = \frac{\kappa'}{\max(e^{0.03\sigma_\alpha})}$, and $\kappa' = 0.4$ is a constant.

3.2. Fusion and Reconstruction

3.2.1 High Frequency Fusion

In complex scenes, images are affected by various interferences. High-frequency components, responsible for details, are sensitive to changes and noise. Noise, a random signal with various frequencies, can obscure information and harm image quality. Thus, high-frequency fusion involves three steps:

Step 1. Adaptive Denoising

First, we calculate the noise level σ_α^h of the high-frequency component, based on noise levels, we decide whether to filter interfering pixels, preserving essential details and edges.

$$OH_\alpha = \begin{cases} \text{SAMF}(H_\alpha, \delta_\alpha, r), & \text{if } \sigma_\alpha^h > 0 \\ H_\alpha, & \text{otherwise} \end{cases} \quad (9)$$

where OH_α denotes the optimized high-frequency components, $\delta_\alpha = 0.4 \times \log_5(\sigma_\alpha^h)$, if $\sigma_\alpha^h = 0$, H_α is directly used as the final optimized high-frequency component FOH_α .

Step 2. Detail Loss Judgment

Image filters reduce noise but may also sacrifice details during high-frequency components fusion. To assess detail loss, we use Kullback-Leibler (K-L) divergence [11] to measure the difference between denoised and original images in terms of detail. A smaller K-L divergence means better preservation of details and edge information in denoised high-frequency components.

Let ρ_α^1 and ρ_α^0 denote represent two probability distributions of H_α and OH_α , respectively, the K-L divergence is calculated as follows:

$$KL(\rho_\alpha^1 \parallel \rho_\alpha^0) = \int \rho_\alpha^1(R) \log \left(\frac{\rho_\alpha^1(R)}{\rho_\alpha^0(R)} \right) dR \quad (10)$$

where R represents the random variable values. By assessing the magnitude of K-L divergence, we gauge grayscale detail pixel similarity between the images, and FOH_α is calculated as follows:

$$FOH_\alpha = \begin{cases} H_\alpha, & \text{if } KL > 0.05 \\ OH_\alpha, & \text{otherwise} \end{cases} \quad (11)$$

Step 3. Significant Information Fusion

The Monogenic phase consistency (MPC) [26] is a superior feature extraction operator that provides precise local phase information, in contrast to traditional phase consistency methods, which are susceptible to noise. The MPC is formulated as follows:

$$MH_\alpha(x, y) = \omega_\alpha(x, y) \left[1 - \gamma \cdot a \cos \left(\frac{E_\alpha(x, y)}{A_\alpha(x, y)} \right) \right] \cdot [E_\alpha(x, y) - T] / (A_\alpha(x, y) + 0.0001) \quad (12)$$

where $E(x, y)$ and $A(x, y)$ are local energy and amplitude sums of $FOH(x, y)$, $\omega(x, y)$ and T represent the weight function and noise compensation factor, and γ is set to 1.5. Next, we introduce weighted fusion rules for obtaining the final high-frequency components FH :

$$FH(x, y) = \sum_{\alpha=1}^3 \left(\frac{MH_\alpha(x, y) + \eta}{\max \left(\sum_{\alpha=1}^3 MH_\alpha(x, y) \right) + \eta} \times H_\alpha \right) \quad (13)$$

where $\eta = 0.1$.

3.2.2 Low-Frequency Fusion

First, we extract energy information from the low-frequency components of the contrast layer and the infrared image, obtaining the energy layer L_4 :

$$L_4 = L_1 \cdot \text{Map}_E + L_3 \cdot (1 - \text{Map}_E) \quad (14)$$

where

$$\text{Map}_E = \begin{cases} 1, & \text{if } L_1 > L_3 \\ 0, & \text{otherwise} \end{cases} \quad (15)$$

The Gabor filter [55] is a versatile linear filter combining Gaussian and sinusoidal functions for feature extraction across scales and directions. To capture low-frequency feature information, we propose a new fusion rule based on Gabor filter. The 2D-Gabor function is defined as:

$$g_\theta = \exp \left(-\frac{x'^2 + \tau^2 y'^2}{2\hat{\sigma}^2} \right) \cos \left(\frac{2\pi x'}{\hat{\lambda}} + \psi \right) \quad (16)$$

where $x' = x \cos \theta + y \sin \theta$ and $y' = -x \sin \theta + y \cos \theta$, $\hat{\lambda} = 20$ denotes the wavelength of the sine, θ denotes the direction of the parallel strips in the Gabor filter kernel, $\theta \in \{0, 45, 90, 135\}$, $\tau = 0.5$ denotes the spatial aspect ratio, $\psi = 0$ denotes the phase shift, and $\hat{\sigma}$ is the standard deviation of the Gaussian envelope.

Subsequently, we can extract the pixel information in four different directions with the Gabor filter:

$$h_\gamma^\theta(x, y) = L_\gamma(x, y) * g_\theta \quad (17)$$

where $\gamma \in \{2, 4\}$, $*$ is the convolution operator, and h_γ^θ is the filtering results in different directions. Then, the significant information can be extracted by calculating the variance V_γ^θ in all directions in h_γ^θ to construct the weight map:

$$V_\gamma^\theta(x, y) = \frac{1}{m \times n} \sum_{x=1}^m \sum_{y=1}^n (h_\gamma^\theta(x, y) - \bar{h}_\gamma^\theta(x, y))^2 \quad (18)$$

where m and n denote the image length and width, respectively, and \bar{h}_γ^θ denotes the mean value of h_γ^θ . The fusion weight map can be calculated as:

$$W_\gamma^L = \frac{V_\gamma^L e^{EN(L_\gamma)}}{e^{EN(L_2)} \cdot V_2^L + e^{EN(L_4)} \cdot V_4^L} \quad (19)$$

where V_γ^L represents the average value of V_γ^θ in all directions and $EN(\cdot)$ represents the image entropy operator [40]. Finally, the low-frequency component fusion results can be obtained according to the fusion weight map W_γ^L :

$$FL = W_2^L \cdot L_2 + W_4^L \cdot L_4 \quad (20)$$

3.2.3 Fusion Result Reconstruction

According to FH and FL , the final fusion result F can be obtained by using the following:

$$F = FH + FL \quad (21)$$

3.3. Why DIPF Can Handle Complex Scenes?

In the proposed algorithm, for the first time, we categorize the pixels in terms of the transmittance of light. As shown in Fig. 5, we observe that in either rain or haze in extreme weather, or noise and overexposure in realistic complex scenes, they affect the degree of light transmittance. And thus, by predicting the image transmittance information, we are able to efficiently separate these interfering pixels from the source image. Since the image features can be effectively classified according to the transmission map, so the proposed method can adaptive extract the interference information in different complex scenes and realise the fusion of different complex scenes.

4. Experiment

4.1. Experimental setup

The RoadScene [52] and M3FD [22] datasets are widely used and they contain 221 and 300 pairs of images, respectively, encompassing challenging scenes like smoke, strong light and rain. In addition, we selected fire scenes in the TNO dataset [46] to add to the comparison experiment. Furthermore, four popular evaluation metrics, including: Q_{MI} , Q_{NCIE} , Q_G and Q_M [23] are used, where a higher score

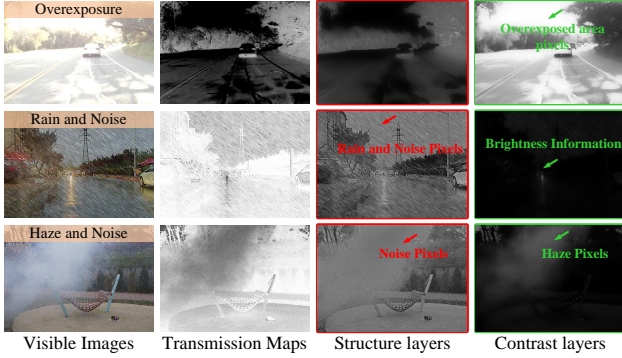


Figure 5. Visualization experiments for effectiveness analysis of decomposition strategy.

represents better fusion performance. Additionally, we selected 11 state-of-the-art comparison methods, they are PFF [63], CDDFuse [60], DeFusion [20], DIVFusion [44], ReCoNet [10], TarDAL [22], MURF [53], LRRNet [16], SEAFusion [42], U2Fusion [52], and UMFusion [49].

4.2. Qualitative comparison

We add Gaussian noise (standard deviation of 20) on both visible and infrared images from the RoadScene dataset, creating A-RoadScene. B-RoadScene simulates conditions with strong interference from bright light sources. We constructed A-M3FD by adding rain and snow [6] to visible images based on M3FD. Additionally, B-M3FD replicates challenging scenes with Gaussian noise (standard deviation of 100) in rainy scene.

Noise Scene Fusion: In Fig. 6, we observe different fusion results in noisy scenes. PFF, MURF, LRRNet, U2Fusion, and UMFusion struggle with image contrast and lose important infrared image luminance. CDDFuse and SEAFusion compensate for lost infrared image texture but introduce noisy pixels from the visible image. Our algorithm excels at preserving infrared image luminance, visible image texture, and reducing noisy pixels.

Overexposure Scene Fusion: In the B-RoadScene dataset presented in Fig. 6, we evaluate various algorithms under overexposure scene. In B-RoadScene, overexposure affects PFF, CDDFuse, ReCoNet and SEAFusion, resulting in the loss of vehicle target information. Our method effectively manages overexposure by balancing visible image energy and infrared thermal radiation, maintaining reasonable contrast in the fused images.

Haze Scene Fusion: In Fig. 6, we assess the performance of different algorithms in scenes affected by haze, where the visibility in visible images is severely reduced. In the magnified red area, all methods successfully incorporate target information from infrared images. However, ReCoNet, MURF, SDDGAN, U2Fusion, and UMFusion ex-

hibit fusion results with poor contrast. PFF, DIVFusion, TarDAL, LRRNet, and SEAFusion struggle to accurately identify smoke as interference.

Rain Scene Fusion: In complex scenes affected by rain, as demonstrated in the test results for A-M3FD and B-M3FD in Fig. 6, various algorithms face challenges. In the zoomed in red area in Rain scene, PFF, DIVFusion, MURF, LRRNet, and U2Fusion encounter difficulties in capturing target information, which struggle to differentiate interfering pixels in the visible image. Combining rainline noise with Gaussian noise presents an even more significant challenge in B-M3FD. With the exception of DeFusion and DIPF, other methods struggle to maintain a reasonable level of contrast across the scene. In Fig. 6, we show the fusion scene with water-damaged visible sensors (Blur). Except for PFF, DIVFusion, MURF, and the proposed method, the others have encountered blur problem.

Snow Scene Fusion: The snow scene in Fig. 6 displays fusion results from various algorithms. In the red area, all methods preserve the snow information in the scene. However, our proposed algorithm excels at minimizing the impact of visible light information in snowy conditions.

Fire Scene Fusion: In the fire scene visualization comparison (Fig. 6), our aim is to accurately locate the fire source and maintain reasonable image contrast. PFF, CDDFuse, and SEAFusion keep excessive visible image information, resulting in overall high brightness and difficulty in fire source detection. In contrast, our algorithm effectively balances both modalities, ensuring visible brightness doesn't interfere with infrared heat source detection.

In summary, our algorithm excels in complex scenes with distractions like haze, snow, rain, noise, overexposure and fire, outperforming 11 SOTA methods.

4.3. Quantitative Comparison

Tab. 1 shows the quantitative comparison results of all the algorithms on seven datasets, where "Average RoadScene" demonstrates the average scores on three datasets, RoadScenen, A-RoadScene, and B-RoadScene, which contain two complex scenarios, noise and overexposure. Average M3FD demonstrates the average score on three datasets, M3FD, A-M3FD and B-M3FD, which contain the four challenges of rain, fog, snow, and noise, while the TNO dataset contains a comparison of fire scenes. It can be seen that the proposed algorithm scores in the top three in a total of 10 metrics in all scenes, and has the best fusion performance in complex scenes.

4.4. Downstream Tasks Experiments

We evaluate the different methods in seven scenes, and four downstream tasks cover semantic segmentation [5], object detection [2], salient object detection [36] and depth estimation [38]. As shown in Fig. 7 and Fig. 8, DIPF has the

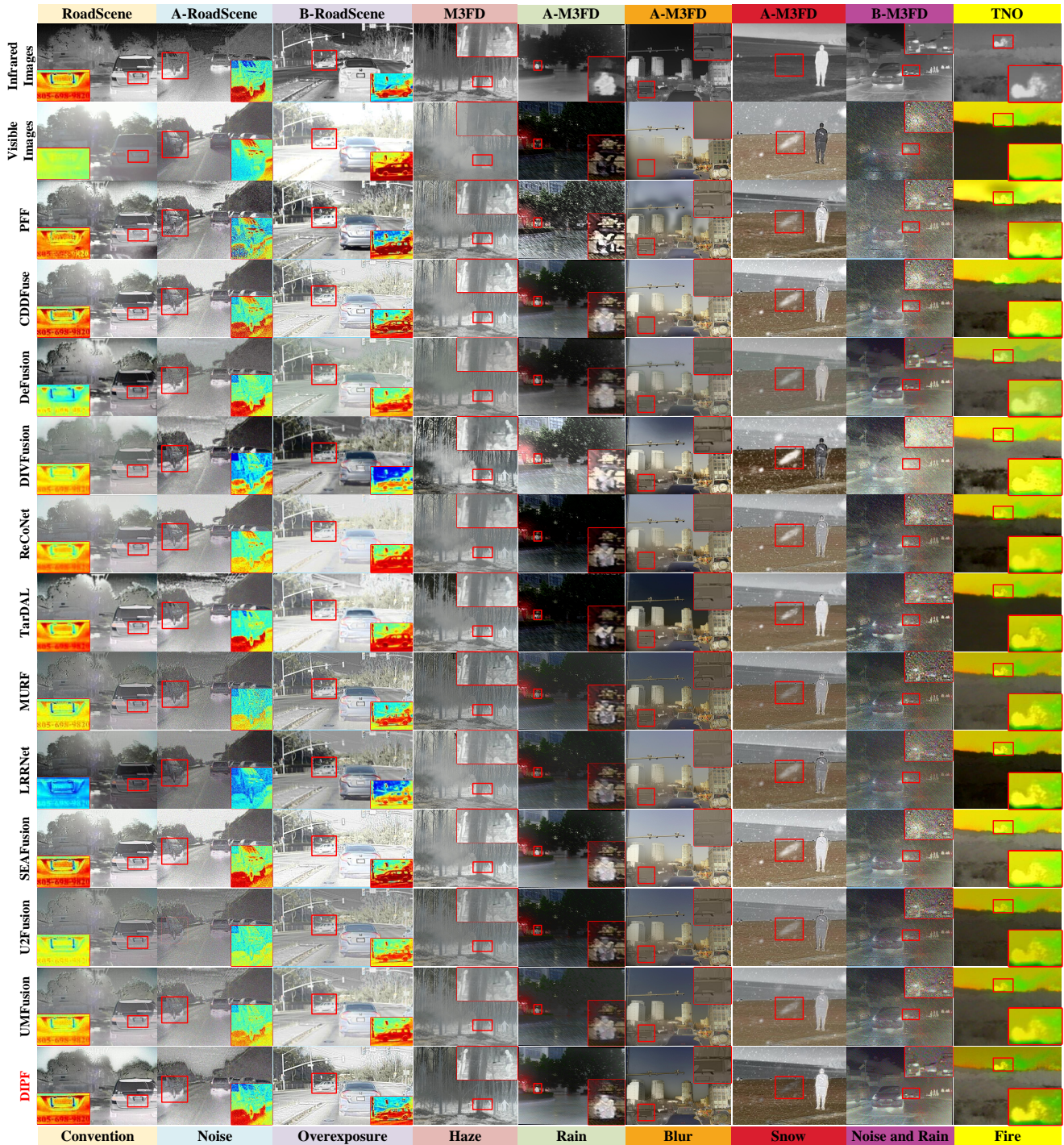


Figure 6. Visual comparison on three scenes. From left to right, conventional, noise, and overexposure scenes.

best performance in the all experiments, proving that it can facilitate downstream tasks under different interferences, integrating useful information from different modal images while being adaptive to interfering pixels. It is worth noting that both UMFusion and CDDFuse methods also showed

good performance in these six sets of experiments.

4.5. Edge Information Evaluation

We use the style migration algorithm [41, 56] to evaluate edge preservation under noise interference. When noise sig-

Table 1. Quantitative comparisons of all methods on six datasets, with "Average RoadScene" and "Average M3FD" denoting the average scores on three datasets each. **Bold** is the best, **Blue** is the second, **Red** is the third.

Methods	Average RoadScene				Average M3FD				TNO			
	$Q_{MI} \uparrow$	$Q_{NCIE} \uparrow$	$Q_G \uparrow$	$Q_M \uparrow$	$Q_{MI} \uparrow$	$Q_{NCIE} \uparrow$	$Q_G \uparrow$	$Q_M \uparrow$	$Q_{MI} \uparrow$	$Q_{NCIE} \uparrow$	$Q_G \uparrow$	$Q_M \uparrow$
PFF	0.2704	0.8049	0.2976	0.2568	0.1691	0.8038	0.1981	0.3004	0.4183	0.8052	0.1795	0.8457
CDDFuse	0.3335	0.8058	0.3017	0.2563	0.3230	0.8069	0.2770	0.3625	0.7746	0.8133	0.3312	1.0995
DeFusion	0.3576	0.8062	0.2707	0.3047	0.5266	0.8050	0.2780	0.3565	0.7344	0.8116	0.2612	0.9169
DIVFusion	0.3489	0.8060	0.2501	0.2686	0.2750	0.8049	0.2054	0.2596	0.6136	0.8087	0.2348	0.7779
ReCoNet	0.4097	0.8067	0.2514	0.3233	0.2882	0.8050	0.2173	0.2716	0.7185	0.8105	0.2703	1.0030
TarDAL	0.3957	0.8070	0.2844	0.3201	0.3244	0.8059	0.1880	0.2421	0.6161	0.8069	0.1455	0.9653
MURF	0.3135	0.8057	0.3417	0.3026	0.2128	0.8042	0.1720	0.2292	0.6615	0.8091	0.3067	0.9396
LRRNet	0.3525	0.8060	0.2588	0.2495	0.2649	0.8049	0.2256	0.2650	0.6630	0.8084	0.2275	0.9794
SeAFusion	0.3374	0.8059	0.3126	0.3022	0.3011	0.8064	0.2662	0.3221	0.7937	0.8136	0.3153	1.0631
U2Fusion	0.3259	0.8057	0.3705	0.3303	0.2407	0.8047	0.2548	0.2760	0.6484	0.8078	0.2318	0.9377
UMFusion	0.3632	0.8067	0.3574	0.3334	0.2695	0.8053	0.2273	0.2659	0.7170	0.8100	0.2019	0.8969
DIPF	0.3703	0.8072	0.3991	0.3930	0.3166	0.8070	0.2793	0.3263	0.6989	0.8418	0.3277	1.0673

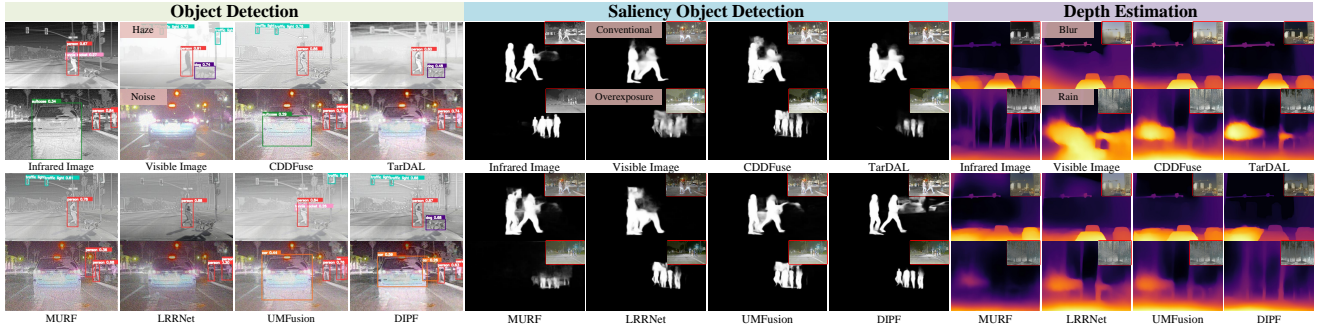


Figure 7. Visualization results of the different algorithms on three downstream tasks.

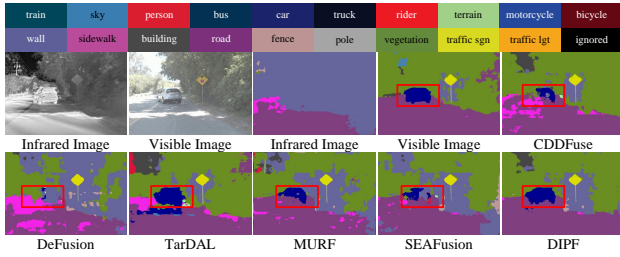


Figure 8. Visual comparison on semantic segmentation.

nificantly obscures edge information, the style migration result deviates from the original scene. As depicted in Fig. 9, when the source image is affected by noise, obtaining an image resembling the original scene becomes challenging. In this set of experiments, only the aforementioned algorithms successfully achieve style migration.

5. Conclusion

In this study, we propose an IVIF method for complex scenes, which can eliminate the interference while obtain cutting-edge fusion performance. We propose a decomposi-

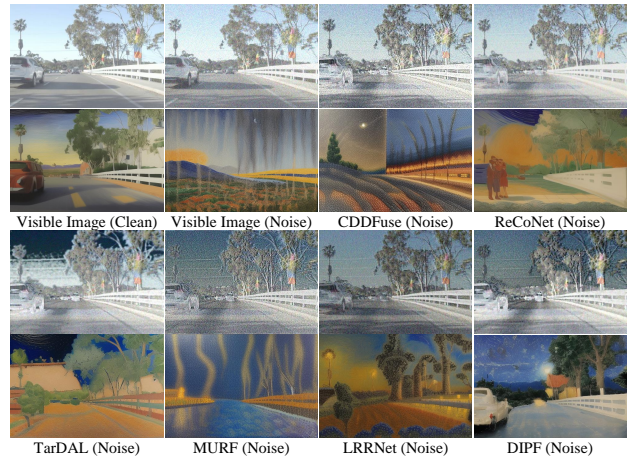


Figure 9. Visual Comparison on style migration.

tion model based on transmittance estimation, and from the perspective of atmospheric light scattering to realize interferential pixels classification. Extensive experiments show that the proposed algorithm produces superior fusion results even under single or multiple interferences.

6. Acknowledgements

This research was supported in part by the National Natural Science Foundation of China under Grant 62201149, in part by the Guangdong Higher Education Innovation and Strengthening of Universities Project under Grant 2023KTSCX127, and in part by the Foshan Key Areas of Scientific and Technological Research Project under Grant 2120001008558.

References

- [1] Codruta O Ancuti, Cosmin Ancuti, and Radu Timofte. Nh-haze: An image dehazing benchmark with non-homogeneous hazy and haze-free images. In *Proceedings of the IEEE/CVF conference on computer vision and pattern recognition workshops*, pages 444–445, 2020. 3
- [2] Alexey Bochkovskiy, Chien-Yao Wang, and Hong-Yuan Mark Liao. Yolov4: Optimal speed and accuracy of object detection. *arXiv preprint arXiv:2004.10934*, 2020. 1, 6
- [3] Nicolas Carion, Francisco Massa, Gabriel Synnaeve, Nicolas Usunier, Alexander Kirillov, and Sergey Zagoruyko. End-to-end object detection with transformers. In *European conference on computer vision*, pages 213–229. Springer, 2020. 1
- [4] Zhihao Chang, Zhixi Feng, Shuyuan Yang, and Quanwei Gao. Aft: Adaptive fusion transformer for visible and infrared images. *IEEE Transactions on Image Processing*, 32: 2077–2092, 2023. 1
- [5] Liang-Chieh Chen, Yukun Zhu, George Papandreou, Florian Schroff, and Hartwig Adam. Encoder-decoder with atrous separable convolution for semantic image segmentation. In *Proceedings of the European conference on computer vision (ECCV)*, pages 801–818, 2018. 6
- [6] Wei-Ting Chen, Hao-Yu Fang, Cheng-Lin Hsieh, Cheng-Che Tsai, I Chen, Jian-Jiun Ding, Sy-Yen Kuo, et al. All snow removed: Single image desnowing algorithm using hierarchical dual-tree complex wavelet representation and contradict channel loss. In *Proceedings of the IEEE/CVF International Conference on Computer Vision*, pages 4196–4205, 2021. 6
- [7] Mina Han, Kailong Yu, Junhui Qiu, Hao Li, Dan Wu, Yujing Rao, Yang Yang, Lin Xing, Haicheng Bai, and Chengjiang Zhou. Boosting target-level infrared and visible image fusion with regional information coordination. *Information Fusion*, 92:268–288, 2023. 1
- [8] Kaiming He, Jian Sun, and Xiaoou Tang. Single image haze removal using dark channel prior. *IEEE transactions on pattern analysis and machine intelligence*, 33(12):2341–2353, 2010. 3
- [9] Yingkun Hou, Jun Xu, Mingxia Liu, Guanghai Liu, Li Liu, Fan Zhu, and Ling Shao. Nlh: A blind pixel-level non-local method for real-world image denoising. *IEEE Transactions on Image Processing*, 29:5121–5135, 2020. 4
- [10] Zhanbo Huang, Jinyuan Liu, Xin Fan, Risheng Liu, Wei Zhong, and Zhongxuan Luo. Reconet: Recurrent correction network for fast and efficient multi-modality image fusion. In *European Conference on Computer Vision*, pages 539–555. Springer, 2022. 2, 6
- [11] Qiuping Jiang, Zhenyu Peng, Guanghui Yue, Hong Li, and Feng Shao. No-reference image contrast evaluation by generating bidirectional pseudoreferences. *IEEE Transactions on Industrial Informatics*, 17(9):6062–6072, 2020. 4
- [12] Alexander Kirillov, Eric Mintun, Nikhila Ravi, Hanzi Mao, Chloe Rolland, Laura Gustafson, Tete Xiao, Spencer Whitehead, Alexander C Berg, Wan-Yen Lo, et al. Segment anything. *arXiv preprint arXiv:2304.02643*, 2023. 1
- [13] Hui Li, Xiao-Jun Wu, and Josef Kittler. Mdlatrr: A novel decomposition method for infrared and visible image fusion. *IEEE Transactions on Image Processing*, 29:4733–4746, 2020. 1
- [14] Huafeng Li, Yueliang Cen, Yu Liu, Xun Chen, and Zhengtao Yu. Different input resolutions and arbitrary output resolution: A meta learning-based deep framework for infrared and visible image fusion. *IEEE Transactions on Image Processing*, 30:4070–4083, 2021. 2
- [15] Hui Li, Xiao-Jun Wu, and Josef Kittler. Rfn-nest: An end-to-end residual fusion network for infrared and visible images. *Information Fusion*, 73:72–86, 2021. 1
- [16] Hui Li, Tianyang Xu, Xiao-Jun Wu, Jiwen Lu, and Josef Kittler. Lrrnet: A novel representation learning guided fusion network for infrared and visible images. *IEEE transactions on pattern analysis and machine intelligence*, 2023. 1, 2, 6
- [17] Huafeng Li, Junzhi Zhao, Jinxing Li, Zhengtao Yu, and Guangming Lu. Feature dynamic alignment and refinement for infrared-visible image fusion: Translation robust fusion. *Information Fusion*, 95:26–41, 2023. 1
- [18] Jiawei Li, Jiansheng Chen, Jinyuan Liu, and Huimin Ma. Learning a graph neural network with cross modality interaction for image fusion. In *Proceedings of the 31st ACM International Conference on Multimedia*, pages 4471–4479, 2023. 2
- [19] Jiale Li, Hang Dai, Hao Han, and Yong Ding. Mseg3d: Multi-modal 3d semantic segmentation for autonomous driving. In *Proceedings of the IEEE/CVF Conference on Computer Vision and Pattern Recognition*, pages 21694–21704, 2023. 1
- [20] Pengwei Liang, Junjun Jiang, Xianming Liu, and Jiayi Ma. Fusion from decomposition: A self-supervised decomposition approach for image fusion. In *European Conference on Computer Vision*, pages 719–735. Springer, 2022. 2, 6
- [21] Jinyuan Liu, Xin Fan, Ji Jiang, Risheng Liu, and Zhongxuan Luo. Learning a deep multi-scale feature ensemble and an edge-attention guidance for image fusion. *IEEE Transactions on Circuits and Systems for Video Technology*, 32(1): 105–119, 2021. 2
- [22] Jinyuan Liu, Xin Fan, Zhanbo Huang, Guanyao Wu, Risheng Liu, Wei Zhong, and Zhongxuan Luo. Target-aware dual adversarial learning and a multi-scenario multi-modality benchmark to fuse infrared and visible for object detection. In *Proceedings of the IEEE/CVF Conference on Computer Vision and Pattern Recognition*, pages 5802–5811, 2022. 1, 2, 5, 6
- [23] Zheng Liu, Erik Blasch, Zhiyun Xue, Jiying Zhao, Robert Laganieri, and Wei Wu. Objective assessment of multiresolution image fusion algorithms for context enhancement in

- night vision: a comparative study. *IEEE transactions on pattern analysis and machine intelligence*, 34(1):94–109, 2011. 5
- [24] Ao Luo, Xin Li, Fan Yang, Zhicheng Jiao, Hong Cheng, and Siwei Lyu. Cascade graph neural networks for rgb-d salient object detection. In *Computer Vision—ECCV 2020: 16th European Conference, Glasgow, UK, August 23–28, 2020, Proceedings, Part XII 16*, pages 346–364. Springer, 2020. 1
- [25] Xiaoqing Luo, Yuting Jiang, Anqi Wang, Juan Wang, Zhancheng Zhang, and Xiao-Jun Wu. Infrared and visible image fusion based on multi-state contextual hidden markov model. *Pattern Recognition*, 138:109431, 2023. 1
- [26] Xue-Gang Luo, Hua-Jun Wang, and Sen Wang. Monogenic signal theory based feature similarity index for image quality assessment. *AEU-International Journal of Electronics and Communications*, 69(1):75–81, 2015. 5
- [27] Jinlei Ma, Zhiqiang Zhou, Bo Wang, and Hua Zong. Infrared and visible image fusion based on visual saliency map and weighted least square optimization. *Infrared Physics & Technology*, 82:8–17, 2017. 1
- [28] Jiayi Ma, Yong Ma, and Chang Li. Infrared and visible image fusion methods and applications: A survey. *Information fusion*, 45:153–178, 2019. 1
- [29] Jiayi Ma, Wei Yu, Pengwei Liang, Chang Li, and Junjun Jiang. FusionGAN: A generative adversarial network for infrared and visible image fusion. *Information fusion*, 48:11–26, 2019. 1
- [30] Jiayi Ma, Hao Zhang, Zhenfeng Shao, Pengwei Liang, and Han Xu. Ganmcc: A generative adversarial network with multiclassification constraints for infrared and visible image fusion. *IEEE Transactions on Instrumentation and Measurement*, 70:1–14, 2020. 1
- [31] Jiayi Ma, Linfeng Tang, Fan Fan, Jun Huang, Xiaoguang Mei, and Yong Ma. Swinfusion: Cross-domain long-range learning for general image fusion via swin transformer. *IEEE/CAA Journal of Automatica Sinica*, 9(7):1200–1217, 2022. 1
- [32] Gaofeng Meng, Ying Wang, Jiangyong Duan, Shiming Xiang, and Chunhong Pan. Efficient image dehazing with boundary constraint and contextual regularization. In *Proceedings of the IEEE international conference on computer vision*, pages 617–624, 2013. 3
- [33] Yan Mo, Xudong Kang, Puhong Duan, Bin Sun, and Shutao Li. Attribute filter based infrared and visible image fusion. *Information Fusion*, 75:41–54, 2021. 1
- [34] Rencan Nie, Chaozhen Ma, Jinde Cao, Hongwei Ding, and Dongming Zhou. A total variation with joint norms for infrared and visible image fusion. *IEEE Transactions on Multimedia*, 24:1460–1472, 2021. 1
- [35] Xuebin Qin, Zichen Zhang, Chenyang Huang, Chao Gao, Masood Dehghan, and Martin Jagersand. Basnet: Boundary-aware salient object detection. In *Proceedings of the IEEE/CVF conference on computer vision and pattern recognition*, pages 7479–7489, 2019. 1
- [36] Xuebin Qin, Zichen Zhang, Chenyang Huang, Masood Dehghan, Osmar R Zaiane, and Martin Jagersand. U2-net: Going deeper with nested u-structure for salient object detection. *Pattern recognition*, 106:107404, 2020. 6
- [37] Suresh Chandra Raikwar and Shashikala Tapaswi. Lower bound on transmission using non-linear bounding function in single image dehazing. *IEEE Transactions on Image Processing*, 29:4832–4847, 2020. 3
- [38] René Ranftl, Katrin Lasinger, David Hafner, Konrad Schindler, and Vladlen Koltun. Towards robust monocular depth estimation: Mixing datasets for zero-shot cross-dataset transfer. *IEEE transactions on pattern analysis and machine intelligence*, 44(3):1623–1637, 2020. 6
- [39] Dongyu Rao, Tianyang Xu, and Xiao-Jun Wu. Tgfuse: An infrared and visible image fusion approach based on transformer and generative adversarial network. *IEEE Transactions on Image Processing*, 2023. 2
- [40] J Wesley Roberts, Jan A Van Aardt, and Fethi Babikker Ahmed. Assessment of image fusion procedures using entropy, image quality, and multispectral classification. *Journal of Applied Remote Sensing*, 2(1):023522, 2008. 5
- [41] Robin Rombach, Andreas Blattmann, Dominik Lorenz, Patrick Esser, and Björn Ommer. High-resolution image synthesis with latent diffusion models. In *Proceedings of the IEEE/CVF conference on computer vision and pattern recognition*, pages 10684–10695, 2022. 7
- [42] Linfeng Tang, Jiteng Yuan, and Jiayi Ma. Image fusion in the loop of high-level vision tasks: A semantic-aware real-time infrared and visible image fusion network. *Information Fusion*, 82:28–42, 2022. 1, 2, 6
- [43] Linfeng Tang, Jiteng Yuan, Hao Zhang, Xingyu Jiang, and Jiayi Ma. Piafusion: A progressive infrared and visible image fusion network based on illumination aware. *Information Fusion*, 83:79–92, 2022.
- [44] Linfeng Tang, Xinyu Xiang, Hao Zhang, Meiqi Gong, and Jiayi Ma. Divfusion: Darkness-free infrared and visible image fusion. *Information Fusion*, 91:477–493, 2023. 1, 2, 6
- [45] Wei Tang, Fazhi He, and Yu Liu. Ydtr: Infrared and visible image fusion via y-shape dynamic transformer. *IEEE Transactions on Multimedia*, 2022. 1
- [46] Alexander Toet et al. Tno image fusion dataset. *Figshare. data*, 2014. 5
- [47] Mikaela Angelina Uy, Ricardo Martin-Brualla, Leonidas Guibas, and Ke Li. Scade: Nerfs from space carving with ambiguity-aware depth estimates. In *Proceedings of the IEEE/CVF Conference on Computer Vision and Pattern Recognition*, pages 16518–16527, 2023. 1
- [48] Chien-Yao Wang, Alexey Bochkovskiy, and Hong-Yuan Mark Liao. Yolov7: Trainable bag-of-freebies sets new state-of-the-art for real-time object detectors. In *Proceedings of the IEEE/CVF Conference on Computer Vision and Pattern Recognition*, pages 7464–7475, 2023. 1
- [49] Di Wang, Jinyuan Liu, Xin Fan, and Risheng Liu. Unsupervised misaligned infrared and visible image fusion via cross-modality image generation and registration. *arXiv preprint arXiv:2205.11876*, 2022. 1, 6
- [50] Lijun Wang, Jianming Zhang, Yifan Wang, Huchuan Lu, and Xiang Ruan. Cliffnet for monocular depth estimation with hierarchical embedding loss. In *European Conference on Computer Vision*, pages 316–331. Springer, 2020. 1

- [51] Wencheng Wang, Xiaohui Yuan, Xiaojin Wu, and Yunlong Liu. Fast image dehazing method based on linear transformation. *IEEE Transactions on Multimedia*, 19(6):1142–1155, 2017. 3
- [52] Han Xu, Jiayi Ma, Junjun Jiang, Xiaojie Guo, and Haibin Ling. U2fusion: A unified unsupervised image fusion network. *IEEE Transactions on Pattern Analysis and Machine Intelligence*, 44(1):502–518, 2020. 1, 2, 5, 6
- [53] Han Xu, Jiteng Yuan, and Jiayi Ma. Murf: Mutually reinforcing multi-modal image registration and fusion. *IEEE Transactions on Pattern Analysis and Machine Intelligence*, 2023. 2, 6
- [54] Hao Zhang, Han Xu, Xin Tian, Junjun Jiang, and Jiayi Ma. Image fusion meets deep learning: A survey and perspective. *Information Fusion*, 76:323–336, 2021. 1
- [55] Lin Zhang, Lei Zhang, Xuanqin Mou, and David Zhang. Fsim: A feature similarity index for image quality assessment. *IEEE transactions on Image Processing*, 20(8):2378–2386, 2011. 5
- [56] Lvmin Zhang, Anyi Rao, and Maneesh Agrawala. Adding conditional control to text-to-image diffusion models. In *Proceedings of the IEEE/CVF International Conference on Computer Vision*, pages 3836–3847, 2023. 7
- [57] Yu Zhang, Yu Liu, Peng Sun, Han Yan, Xiaolin Zhao, and Li Zhang. Ifcnn: A general image fusion framework based on convolutional neural network. *Information Fusion*, 54: 99–118, 2020. 1
- [58] Fan Zhao, Wenda Zhao, and Huchuan Lu. Interactive feature embedding for infrared and visible image fusion. *IEEE Transactions on Neural Networks and Learning Systems*, 2023. 1
- [59] Zixiang Zhao, Shuang Xu, Chunxia Zhang, Junmin Liu, and Jianshe Zhang. Bayesian fusion for infrared and visible images. *Signal Processing*, 177:107734, 2020. 1
- [60] Zixiang Zhao, Haowen Bai, Jianshe Zhang, Yulun Zhang, Shuang Xu, Zudi Lin, Radu Timofte, and Luc Van Gool. Cddfuse: Correlation-driven dual-branch feature decomposition for multi-modality image fusion. In *Proceedings of the IEEE/CVF Conference on Computer Vision and Pattern Recognition*, pages 5906–5916, 2023. 1, 2, 6
- [61] Huabing Zhou, Wei Wu, Yanduo Zhang, Jiayi Ma, and Haibin Ling. Semantic-supervised infrared and visible image fusion via a dual-discriminator generative adversarial network. *IEEE Transactions on Multimedia*, 2021. 1
- [62] Zhiqiang Zhou, Bo Wang, and Jinlei Ma. Scale-aware edge-preserving image filtering via iterative global optimization. *IEEE Transactions on Multimedia*, 20(6):1392–1405, 2017. 4
- [63] Zhiqiang Zhou, Erfang Fei, Lingjuan Miao, and Rao Yang. A perceptual framework for infrared–visible image fusion based on multiscale structure decomposition and biological vision. *Information Fusion*, 93:174–191, 2023. 1, 2, 6